Draft version July 2, 2021
Typeset using LaTeX **twocolumn** style in AASTeX62

First observation of MeV gamma-ray universe with true imaging spectroscopy using the Electron-Tracking Compton Telescope aboard SMILE-2+

Atsushi Takada,[1] Taito Takemura,[1] Kei Yoshikawa,[1] Yoshitaka Mizumura,[2] Tomonori Ikeda,[1] Yuta Nakamura,[1] Ken Onozaka,[1] Mitsuru Abe,[1] Kenji Hamaguchi,[3] Hidetoshi Kubo,[1] Shunsuke Kurosawa,[4] Kentaro Miuchi,[5] Kaname Saito,[1] Tatsuya Sawano,[6] and Toru Tanimori[1]

[1] *Graduate School of Science, Kyoto University*
Kitashirakawa Oiwakecho, Sakyo, Kyoto, Kyoto, 606-8502, Japan
[2] *Institute of Space and Astronautical Science, Japan Aerospace Exploration Agency*
Yoshinodai 3-1-1, Chuou, Sagamihara, Kanagawa, 252-5210, Japan
[3] *Department of Physics, University of Maryland, Baltimore County*
1000 Hilltop Circle, Baltimore, MD 21250, USA
[4] *Institute of Materials Research, Tohoku University*
Katahira 2-1-1, Aoba, Sendai, Miyagi, 980-8577, Japan
[5] *Graduate School of Science, Kobe University*
1-1 Rokkoudai-cho, Nada-ku, Kobe, Hyogo, 657-8501, Japan
[6] *Graduate School of Natural Science and Technology, Kanazawa University*
Kakuma, Kanazawa, Ishikawa, 920-1192, Japan

ABSTRACT

MeV gamma-ray is a unique window for the direct measurement of line emissions from radioisotopes, but there is no significant progress in the observation after COMPTEL/*CGRO*. Hence, for observing celestial objects in this band, we are developing an electron-tracking Compton camera (ETCC), which enables us to perform true imaging spectroscopy similar to X-ray or GeV telescopes. Therefore, we can obtain the energy spectrum of the observation target by a simple ON-OFF method using the correctly defined a proper point-spread function. For validating the performance of celestial object observation using an ETCC, the second balloon SMILE-2+, which had an ETCC based on a gaseous electron tracker with a volume of $30\times30\times30$ cm^3, was launched at Alice Springs, Australia on April 7, 2018. SMILE-2+ observed the southern sky including the Crab nebula with a live time of 5.1 h at the zenith angle of $\sim$50 degrees and detected gamma-rays from the Crab nebula with a significance of 4.0σ at the energy range of 0.15–2.1 MeV. Additionally, an enhancement of gamma-ray events due to the Galactic center region was clearly observed in the light curve. The realized detection sensitivity agrees well with the sensitivity estimated before launching based on the total background of extragalactic diffuse, atmospheric gamma-rays, and a small number of instrumental gamma-rays suppressed to one-third of the total background. We have succeeded to overcome the most difficult and serious problem of huge background for the stagnation of MeV gamma-ray astronomy for the first time in the world, and thus demonstrate that an ETCC can pioneer a deeper survey than COMPTEL in MeV gamma-ray astronomy.

Keywords: Gamma-ray astronomy — Gamma-ray telescopes — High altitude balloons

1. INTRODUCTION

In the low-energy gamma-ray band of 0.1–100 MeV, we can observe various radiation processes in universe, such as the line emission from the radioisotopes produced by the nucleosynthesis in the supernovae or the neutron star mergers (Matz et al. 1988; von Ballmoos 1995), the electron–positron annihilation line in the Galactic center region (GCR) (Prantzos et al. 2011), the synchrotron emission and inverse Compton scattering with particle acceleration in active galactic nuclei or gamma-ray bursts (GRBs) (Urry & Padovani 1995; Briggs et al. 1999), the pion-decay radiation in

Corresponding author: Atsushi Takada
takada@cr.scphys.kyoto-u.ac.jp

the strong gravity field around black holes (McConnell et al. 1996; Mahadevan et al. 1997), the de-excitation lines from the excited nuclei by the interactions between cosmic-rays and interstellar medium (Boggs et al. 2000; Strong et al. 2000). Population III stars are expected to be detected as long duration GRBs (Mészáros & Rees 2010; Toma et al. 2011), because the universe is very transparent in this energy band. If primordial black holes (PBHs) having the mass of 10^{16-17} g exist, the thermal emission may appear in the extragalactic diffuse emission because such PBHs emit the thermal gamma-ray emissions in MeV band (Carr et al. 2010).

Although observations of celestial MeV gamma-rays started in the dawn of the high-energy astrophysics, similar to the discovery of GRBs by *Vela* and the detection of extragalactic diffuse emission by *Apollo 15* (Trombka et al. 1973), the observations in this band have not been advanced thus far. COMPTEL aboard *CGRO* (Schönfelder et al. 1993) discovered only ∼30 steady gamma-ray sources in 0.75–30 MeV (Schönfelder et al. 2000), and SPI loaded on *INTEGRAL* discovered only four steady celestial objects at the energy above 0.6 MeV (Bouchet et al. 2008). In supernova explosions, line gamma-rays emitted from fresh isotopes are expected; however, line gamma-rays emitted from ^{56}Ni/^{56}Co were barely detected with only SN1987A (Matz et al. 1988) and SN2014J (Diehl et al. 2015; Chrazov et al. 2015). Various gamma-ray telescopes are being currently developed and some balloon experiments have already been performed, but no observation have clearly indicated the possibility of these telescopes having better sensitivity than that of COMPTEL (Aprile et al. 2008; Bandstra et al. 2011; Kamiya 2011).

The reason of stagnation in MeV observations is the huge background and the difficulty of imaging. The wavelength of MeV gamma-ray is too short to focus using a mirror or a lens similar to that performed in the observation of visible light or X-rays. Obtaining the total energy is also difficult because most of the incident photons deposit only partial energy via Compton scattering, which is the dominant process between MeV gamma-rays and material. In addition, the observations are obstructed by huge background photons produced by the hadoronic interactions between cosmic rays and the material surrounding the detector (Weidenspointner et al. 2001). The detectors based on the coded aperture imaging, which is the basis of SPI, infer the intensity map of incident gamma-rays using the pattern of the shadow image. Thus they need many photons to obtain the direction of the celestial objects. The coded aperture imaging telescope usually has an active veto counter, but the heavy anti-coincidence counters scarcely improve the signal to noise ratio because of the delayed gamma-rays produced by cosmic-rays (Diehl et al. 2018). Conventional Compton cameras such as COMPTEL can slightly suppress the contamination of background photons by the partially restriction of the incident direction for each photon. However, this type of camera measures only one of two angles representing the direction of incident gamma-ray. Thus, the detection sensitivity is not improved by the large contamination of background gamma-rays (e.g., extragalactic diffuse emission) because the point spread function (PSF) of the conventional Compton camera is extended to the average of the detectable scattering-angle due to the lack of recoil direction(Tanimori et al. 2017). Actually, Schönfelder (2004) argue that the most important ability of next MeV gamma-ray telescope is background rejection based on the sharp PSF and the additional event-selection parameters.

As the next MeV gamma-ray telescope for the deep sky survey, we are developing an electron-tracking Compton camera (ETCC), which consists of a gaseous electron tracker as a Compton-scattering target and the pixel scintillator arrays as the absorbers (Tanimori et al. 2004). The difference between ETCC and the conventional Compton camera is the tracking of Compton-recoil electron. The developed ETCC can reconstruct Compton scattering process completely by obtaining the momentum of the incident gamma-ray with the simple summation of the momenta of the scattered gamma-ray and the recoil electron, event by event. Thus, ETCC can provide a proper PSF same as telescopes in other wavelength telescopes, which enables us to obtain the energy spectrum of the observation target by the simple ON-OFF method (Tanimori et al. 2017). Moreover, the recoil electron track provides two powerful background rejection tools (Tanimori et al. 2015). One is particle identification based on the energy deposition rate dE/dx in the gaseous electron tracker, and the other is Compton-scattering kinematic test using the angle between the directions of scattering gamma-ray and recoil electron. A heavy veto-counter is not necessary for the observation using the ETCC because of these background rejection tools; thus, the ETCC has a large field of view (FoV). Therefore, these unique abilities of ETCC providesa real imaging spectroscopy to MeV gamma-ray observations. For the future observations with ETCCs loaded on a satellite (Hamaguchi et al. 2019), we have a plan of the balloon experiments, named Sub-MeV/MeV gamma-ray Imaging Loaded-on-balloon Experiments (SMILE). As the first step, we launched a small ETCC having an electron tracker with a sensitive volume of 10×10×15 cm^3 for the background study at

high altitudes in 2006 (SMILE-I) and the confirmation of the background rejection power of the ETCC (Takada et al. 2011). SMILE-I was successful in detecting diffuse cosmic and atmospheric gamma-rays with powerful background rejection based on particle identification. The second step of SMILE is the confirmation of imaging spectroscopy with observations of bright celestial objects. To this end, we set the Crab nebula and GCR as the observation targets, and constructed a middle-size ETCC having a sensitive volume of $30\times30\times30$ cm^3 for 3–5σ level significant detection of the Crab nebula by assuming the background to be constructed of extra-galactic diffuse and atmospheric gamma-rays. The second balloon SMILE-2+ was launched at Alice Springs, Australia, on April 7, 2018.

Herein, we report the gamma-ray detection abilities with the ground calibrations, details of SMILE-2+ flight, and the observation result of the Crab nebula; in addition, we discuss the detection sensitivities of next observation with ETCCs by comparing the realized detection sensitivity with the estimation based on the ground calibrations.

2. INSTRUMENTS

2.1. *SMILE-2+ ETCC and control system*

At the middle latitude in the southern hemisphere, the flux of the Crab nebula is deceased by a half due to its large zenith angle of more than 45 degrees, which increases the air mass twice than the zenith. Thus, it is not easy to detect even the Crab nebula in several hours of balloon observation. To detect the Crab nebula with a significance of 3–5σ during a few hours in the energy band of 0.2–2 MeV at an altitude of 40 km in the southern hemisphere, we need an ETCC with an effective area of at least $\sim$1 cm^2 for 0.3 MeV, a PSF of $\sim$30 degrees for 0.6 MeV at the half power radius (HPR), and the suppression of the instrumental background to the amount less than that of the diffuse cosmic and atmospheric gamma-rays. Figure 1 shows the schematic view of SMILE-2+ ETCC. A good material for a Compton-scattering target should have a high electron-density for a high Compton-scattering probability and a low atomic-number for suppression of photoabsorption. For this purpose, the electron tracker of SMILE-2+ ETCC has a sensitive volume of $30 \times 30 \times 30$ cm^3 filled by an argon-based gas (Ar : CF_4 : iso C_4H_{10} = 95 : 3 : 2 in pressure ratio) with the pressure of 2 atm. The drift velocity of electron in this gas is approximately 3.7 cm μs^{-1}. We adopted a time projection chamber (TPC) using a micro pixel chamber (μ-PIC) (Ochi et al. 2001; Takada et al. 2005) and a gas electron multiplier (Sauli 1997; Tamagawa et al. 2006) having an insulator of 100 μm liquid crystal polymer because the ETCC needs the three-dimensional (3D) precise electron tracks for the gamma-ray reconstruction. The readout pitch of this tracker is 800 μm as two adjacent readout-strips of μ-PIC were combined to one preamplifier for reducing the power consumption. The energy resolution of the tracker in the whole volume is 45.9% for 0.043 MeV (GdKα) at full-width half maximum (FWHM). As the gamma-ray absorber, we use GSO (Gd_2SiO_5:Ce) pixel scintillator arrays (PSAs), which contain 8×8 pixels with a pixel size of 6×6 mm^2. The thickness of GSO scintillator is 26 and 13 mm at the bottom and side of the electron tracker, respectively. For the efficient absorption of the scattered gamma-rays, we placed 36 PSAs at the bottom and 18 PSAs at each side of the tracker, such that the number of scintillation pixels is 6912 pixels. As the photo readout, we adopted the 4-ch charge division method with the resistor network (Sekiya et al. 2006) and the multi-anode photo multiplier tubes (Hamamatsu Photonics, flat-panel H8500). The energy resolutions of the bottom and the side PSAs are 13.4% and 10.9% for 0.662 MeV at FWHM, respectively. The pixel scintillator arrays are placed in the TPC vessel, whereas the scintillators of the previous ETCC including SMILE-I were placed at the outside of the vessel.

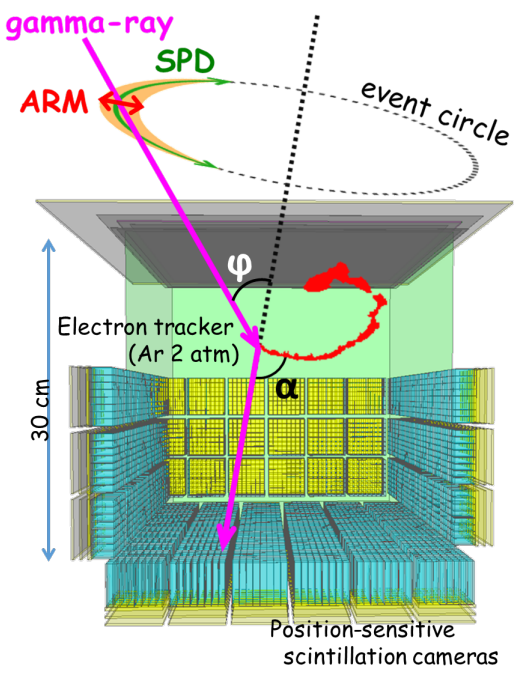

Figure 1. Schematic view of the electron-tracking Compton camera (ETCC). The ETCC comprises a gaseous electron tracker as a Compton-scattering target and position-sensitive scintillation cameras as the absorbers for scattered gamma-rays.

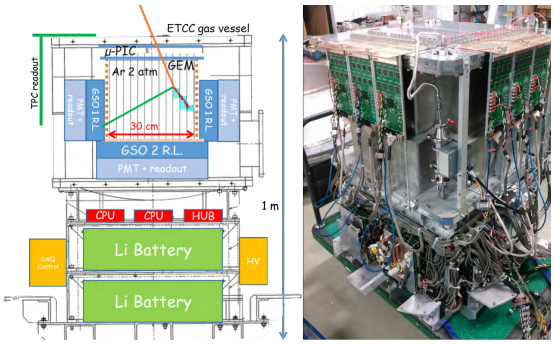

Figure 2. Cross-sectional view (left) and photograph (right) of SMILE-2+ system. Upper and lower halves are the ETCC and the control system, respectively.

Total number of readouts are 768 ch for TPC and 432 ch for PSAs. The data acquisition system of SMILE-2+ is almost the same as that of the middle-size ETCC prototype (Mizumoto et al. 2015); however, we adopted the gigabit Ethernet link instead of the VME bus for fast data transference. At the top of TPC vessel, there is a 5 mm-thick plastic scintillator for reducing the triggers by the charged particles.

The SMILE-2+ ETCC is set above the control system, as shown in Fig. 2. The control system has one CPU for communication with the balloon control system, two CPUs with 1 TB SSDs for data acquisition, a trigger control unit described in Mizumoto et al. (2015), four high-voltage units for the TPC, a power management system with DC/DC converters, and the lithium batteries. SMILE-2+ also has a GPS receiver, an atmospheric pressure gauge, two clinometers, and three geomagnetic aspectmeters (GAs) for measuring the gondola attitude; however, there is no feedback system for the attitude control. The accuracy of posture measurements is less than 5 degrees. Total power consumption is approximately 250 W provided by the lithium batteries. The SMILE-2+ system is sealed in the pressured vessel maintained at 1 atm. The side of the outer vessel is covered by the multilayered insulators for maintaining the temperature, and the outer vessel is placed on the small aluminum gondola, as shown in Fig. 3. The total weight of SMILE-2+ gondola without ballast is 511 kg.

2.2. *ground calibration*

Our ETCC obtains the 3D track and the energy of the Compton-recoil electron using the gaseous electron tracker, whereas the absorber detects the absorption point and the energy of the Compton-scattered gamma-ray. Then, we can reconstruct the momentum of the incident gamma-ray by summing the momenta of both the recoil electron and the scattered gamma-ray,

$$p_0^\mu = p_\gamma^\mu + p_e^\mu, \tag{1}$$

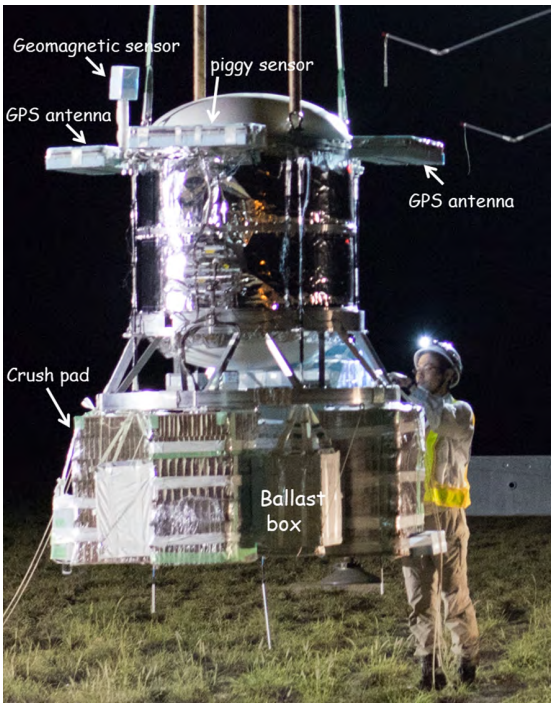

Figure 3. Photograph of SMILE-2+ gondola.

where p_0^μ, p_γ^μ, and p_e^μ are the four-dimensional momenta of the incident gamma-ray, scattered gamma-ray, and recoil electron, respectively. Using the measured values, the unit vector of the incident gamma-ray $\mathbf{r}$ is described by

$$\mathbf{r} = \left(\cos\phi - \frac{\sin\phi}{\tan\alpha}\right)\mathbf{g} + \frac{\sin\phi}{\sin\alpha}\mathbf{e}, \tag{2}$$

where $\mathbf{g}$ and $\mathbf{e}$ are unit vectors in the directions of the scattered gamma-ray and the recoil electron in laboratory system, respectively. α is the angle between the scattering and recoil directions as shown in Fig. 1, and ϕ is the scattering angle given by

$$\cos\phi = 1 - m_e c^2 \left(\frac{1}{E_\gamma} - \frac{1}{E_\gamma + K_e}\right), \tag{3}$$

where E_γ, K_e, m_e, and c are the energy of the scattered gamma-ray, kinetic energy of the Compton-recoil electron, electron mass, and light speed, respectively.

We specify the fully-reconstructed gamma-ray candidate events with the criteria as follows.

1. Single pixel scintillator hit: When the Compton-scattered gamma-ray hits more than one pixel in the absorber, reconstructing the incident gamma-ray is difficult because it could confuse the sequence of the interactions in the absorber. Therefore we select the events with a single pixel scintillator hit.

2. Fully-contained electron: For gamma-ray reconstruction, we need the kinetic energy of a recoil electron. If the recoil electron escapes out of the sensitive volume of the TPC, we miss the reconstruction of the incident gamma-ray owing to the incomplete measurement of the recoil energy. Then we set the TPC fiducial volume of $29\times29\times29$ cm^3 and require that the track length matches the range of electron in Ar gas expected by the deposited energy (Tanimori et al. 2015). Figure 4 shows the track length of the charged particle detected at the level flight as a function of the deposited energy in the TPC. The gradient in this figure represents the energy loss dE/dx. We select the events in the hatched area for the fully-contained electrons. In addition, we decide the head-tail of recoil electron using the skewness of the track image (Dujmic et al. 2008), and the recoil direction using the time-over-threshold information (Tanimori et al. 2015). The angular resolution of recoil direction and the position resolution of scattering points are described as the traditional method in Ikeda et al. (2021).

3. Compton scattering kinematics: α is defined by

$$\cos\alpha_g = \mathbf{g}\cdot\mathbf{e}, \tag{4}$$

and is also calculated with the Compton-scattering kinematics as follows:

$$\cos\alpha_k = \left(1-\frac{m_e c^2}{E_\gamma}\right)\sqrt{\frac{K_e}{K_e+2m_e c^2}}. \tag{5}$$

Therefore, we can select only Compton scattering events with the condition described by

$$|\cos\alpha_g - \cos\alpha_k| \le \Delta_\alpha, \tag{6}$$

where Δ_α is a cut parameter. For SMILE-2+ ETCC, we set $\Delta_\alpha = 0.5$.

We constructed a simulator of SMILE-2+ ETCC based on Geant4 (ver 10.04-patch02; Agostinelli et al. 2003) to obtain the response function for parallel light, which is required in the deconvolution of gamma-ray fluxes from celestial objects. We adopted G4EmLivermorePhysics to calculate electromagnetic interaction with considering Doppler broadening in Compton scattering. To confirm the reliability of the SMILE-2+ ETCC simulator, we measured the effective area, PSF, and energy resolution under the irradiation of line gamma-rays from the checking sources, which were placed at the distance of approximately 2 m from the center of SMILE-2+ ETCC, and we compared the measured performance with the simulation expectations.

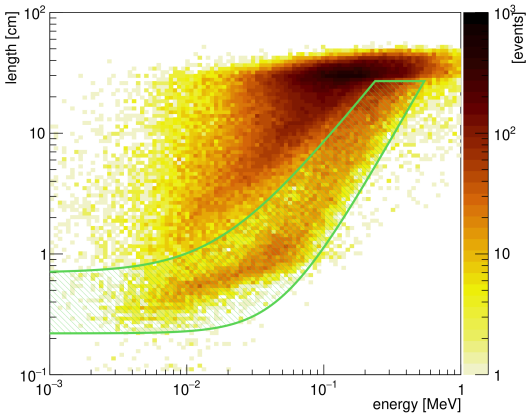

Figure 4. Track length of charged particles as a function of deposited energy in SMILE-2+ TPC. We selected the fully-contained electron events inside the hatched green area.

Figure 5 shows the effective area as a function of the incident energy in the case of the checking sources on the center axis of the ETCC or the parallel light with a zenith angle of 0 degrees. Based on this figure, it is noted that the expected effective areas are consistent with the measured ones. The realized effective area with the energy selection is 1.1 cm^2 at 0.356 MeV, which satisfies the criterion for the detection of the Crab nebula. In contrast, the difference between the all reconstructed events and the energy-selected events (twice of FWHM at full-energy peak) becomes larger with the higher energy. This difference is caused by the scattered component, which is the scattered gamma-ray in the surrounding material (e.g., pressured vessel, TPC vessel, support structure for PSAs) before the incoming into the ETCC. Typically, the observations of MeV gamma-rays are considered to be confused by not only the expected contamination with the PSF blurring of surrounding sources but also the scattered component from the structures, as the major interaction is Compton scattering. An accurate response function is critical for obtaining the true fluxes of celestial objects. The zenith angle dependence of the effective area for 0.662 MeV is shown in Fig. 6. The SMILE-2+ ETCC field of view, defined as a field with more than half of the effective area at the zenith, is large at 3.1 sr. This ETCC simulator describes the effective area with an accuracy better than 10% at the energy range of 0.15–2.1 MeV within the FoV. Half-power radius (HPR) of PSF as a function of the incident energy is shown in Fig. 7. The PSF size of SMILE-2+ ETCC is 30 degrees for 0.662 MeV at HPR. Further, the angular resolution measure (ARM), which is the accuracy of the scattering angle, and the scatter plane deviation (SPD), which

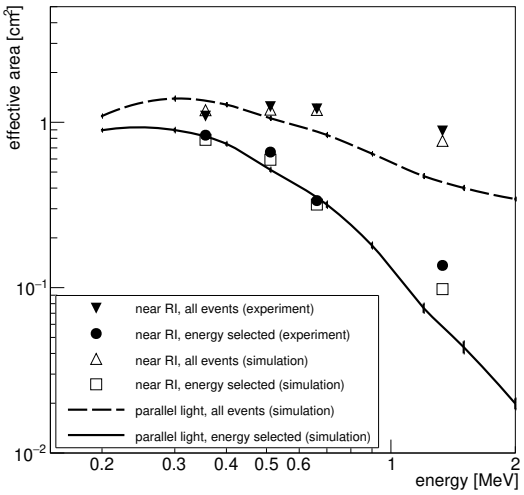

Figure 5. Effective area as a function of the incident energy. Filled- and opened-triangles represent the effective area of all reconstructed events obtained via the experiments and simulation, respectively. After the energy selection at FWHM, each effective area becomes filled-circles (experiments) and opened-squares (simulation). For parallel light, the effective area of all events and energy-selected events are shown with dashed and solid lines, respectively.

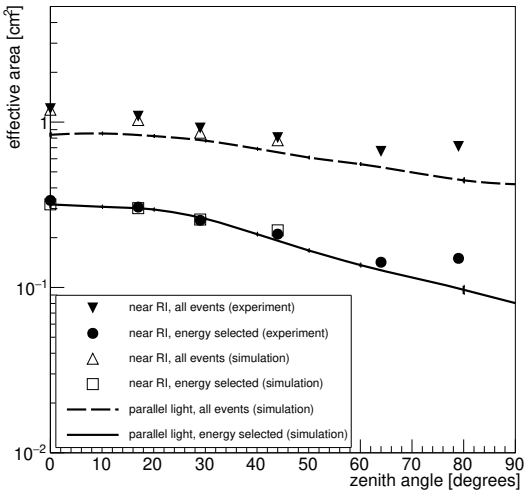

Figure 6. Zenith angle dependence of the effective area for the incident energy of 0.662 MeV. Symbols are same as those in Fig. 5.

is the accuracy of the scattering plane, are 10.5 and 148 degrees for 0.662 MeV at FWHM, respectively. The PSF of the ETCC depends on the energy resolution of PSAs, the position accuracy of the Compton-scattering point, and the angular resolution of the direction of Compton-recoil electron. Although SMILE-2+ ETCC does not have a good spatial resolution compared with

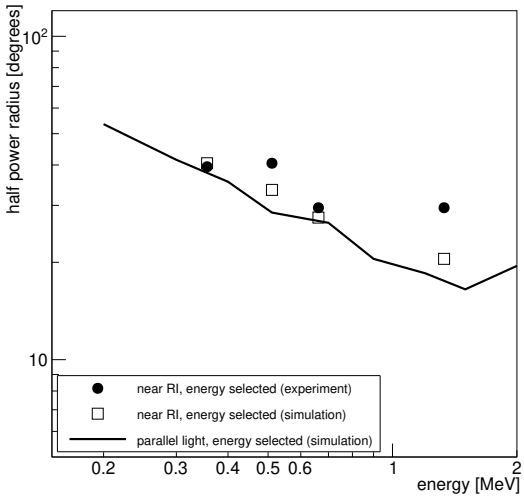

Figure 7. Half-power radius (HPR) of PSF as a function of the incident energy. The filled-circles, opened-squares, and solid line represent measured HPR utilizing the checking sources, simulated HPR with the near point source, and simulated HPR for parallel light.

advanced telescopes in the other wavelengths, it satisfies the criteria for the detection of the Crab nebula with powerful background rejection capability. Figure 8 shows the energy resolution of SMILE-2+ ETCC, TPC and PSA. The fully-contained electron events are limited to the recoil energy of lower than 0.3 MeV for lack of a stopping power of the TPC gas. Therefore the energy of the scattered gamma-ray becomes larger than that of the recoil electron such that the energy resolution of the ETCC is dominated by that of PSAs.

3. SMILE-2+ BALLOON FLIGHT

The SMILE-2+ balloon was launched by ISAS/JAXA from Australian balloon launch station, Alice Springs, Australia, on April 7, 2018 at 06:24 Australian Central Standard Time (ACST). The SMILE-2+ system was switched on 3 h prior to the launch, and data acquisition was running even during the ascent. The time variations of the altitude and atmospheric pressure are shown in the upper and lower panels of Fig. 9, respectively. At 08:44 ACST, the balloon reached an altitude of 39.6 km. SMILE-2+ performed the observation until 10:45 ACST on April 8, and was switched off at 10:53 ACST. At 06:30 ACST on April 8, 2018, the balloon slightly ascended owing to sunrise. The duration of the level flight, in which the atmospheric depth was maintained between 2.4–3.8 hPa (altitude 37.8–40.4 km), was approximately 26 h. On April 9, 2018, we approached to the gondola, which landed at a distance of approximately 190 km from Alice Springs, and successfully recovered the SMILE-2+ gondola.

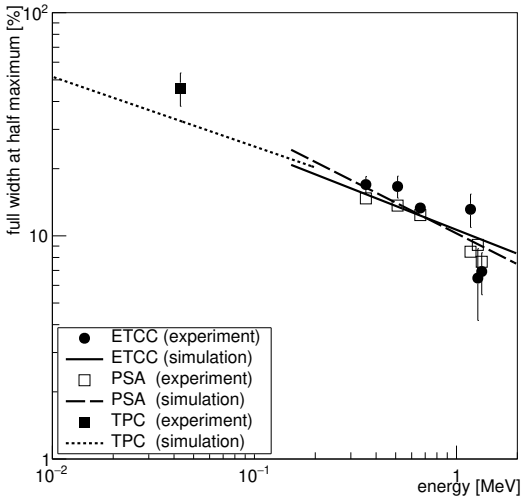

Figure 8. Energy resolutions of ETCC, TPC, PSAs as the functions of the energy. The filled-circle and solid line represent the energy resolution of the SMILE-2+ ETCC obtained via ground calibration and simulation, respectively. The filled-square and opened-square are the averaged energy resolution of TPC and PSAs, respectively, measured via ground calibration, and the dotted and dashed line represent the energy resolution of TPC and PSA in simulation, respectively.

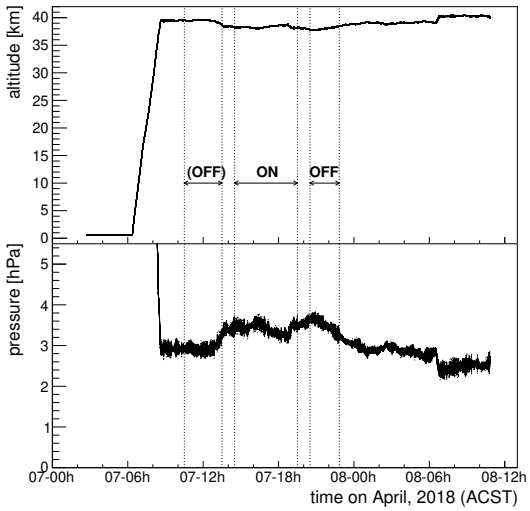

Figure 9. Time variation of the altitude of SMILE-2+ gondola (upper panel) and atmospheric pressure (lower panel).

Figure 10 shows the flight path of SMILE-2+ balloon until the turn-off of the SMILE-2+ system. The contours in Fig. 10 represents the cutoff rigidity calculated by PARMA (Sato et al. 2008) based on MAGNETOCOSMICS (Desorgher et al. 2005). The time-averaged cutoff rigidity is 8.2±0.4 GV during the level flight, and K_p index, which is an indicator of the disturbances in the

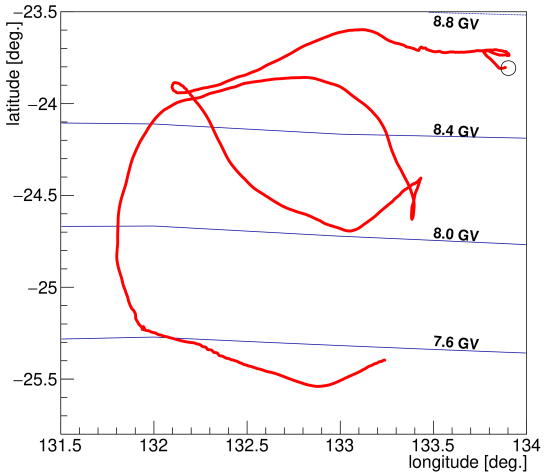

Figure 10. Flight path of SMILE-2+. Opened circle represents the position of Australian balloon launch station, and the contours are the cutoff rigidity calculated by PARMA (Sato et al. 2008).

Earth's magnetic field, is below 2[1]. Thus, the magnetic field condition is stable and quiet, and the intensities of cosmic-rays are considered to have negligible fluctuations in the SMILE-2+ observation. In contrast, the intensity of atmospheric gamma-ray is proportional to $zR_{\rm cut}^{-1.13}$ (Schönfelder et al. 1977; Thompson et al. 1981), where z and $R_{\rm cut}$ are the atmospheric depth and the cutoff rigidity, respectively. The balloon altitude decreased between 13:32–23:00 ACST on April 7, 2018, as shown in Fig. 9, such that the intensity of atmospheric gamma-ray is expected to rise because of an approximately 20% increase of the atmospheric depth.

Time variations of the elevation angles and air masses of the observation targets are shown in Fig. 11 a) and b), respectively. SMILE-2+ observed the Crab nebula and the Galactic center for 5.1 h and 10.2 h in live time, respectively. Figure 12 represents the exposure map with the definition of the observation area by the zenith angle below 60 degrees. Figure 11 c) shows the count rates of PSAs, TPC, and ETCC. The data acquisition rate shown in red in Fig. 11 was 40 Hz on ground, 700 Hz near the Pfotzer maximum (live time 45%), and approximately 450 Hz at an altitude of 39.6 km. After 06:45 ACST on April 8, 2018, the count rate of TPC became high, because the TPC started to suffer from small discharges. However, these discharge events can be clearly discriminated from charged particle tracks using the track images, and thus the discharge events do

[1] https://www.gfz-potsdam.de/en/kp-index

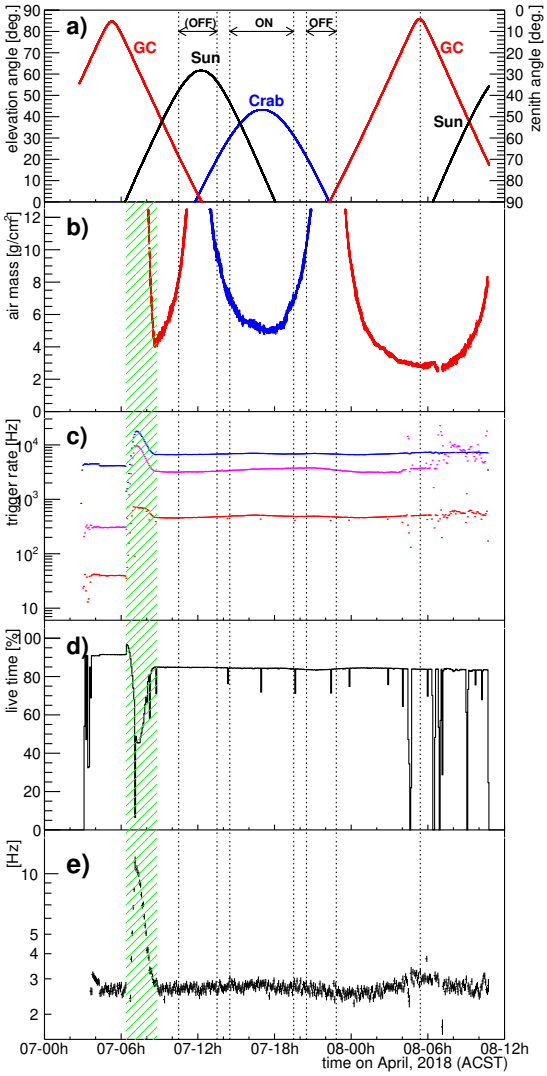

Figure 11. Time variations of a) elevation angles and b) air mass during SMILE-2+ experiment. Red, blue, and black represent the Galactic center, the Crab nebula, and the Sun, respectively. c) Count rates of PSAs (blue), TPC (magenta), and ETCC (red) as the functions of time. Live time of the data acquisition is shown in d). e) shows the light curve obtained by the gamma-ray reconstruction and live-time correction. This light curve is the total event rate of final-remaining gamma-ray in all direction. The hatched area in b), c), d), and e) represents the balloon ascending period.

not disturb the gamma-ray observation. The live time depending on the time is shown in Fig. 11 d). During level flight, the live time of the data-acquisition was maintained above 82% which was enough to observe the Crab nebula and Galactic center.

4. ANALYSIS

4.1. *gamma-ray reconstruction*

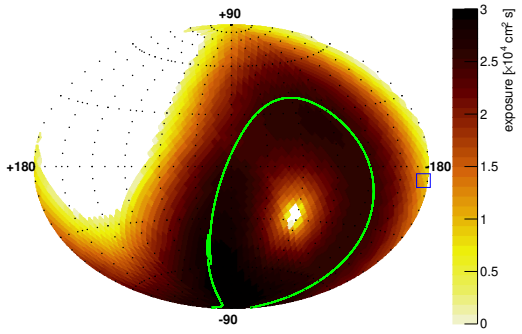

Figure 12. Exposure map for 0.3 MeV in the galactic coordinates with a zenith angle less than 60 degrees. The solid line and opened square represent the track of the light axis of SMILE-2+ ETCC and the Crab nebula, respectively.

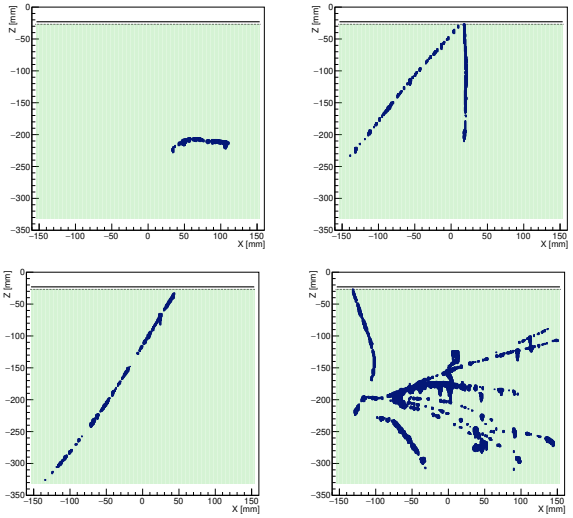

Figure 13. Typical tracks obtained by SMILE-2+ during the level flight. (left-top: single electron, right-top: pair-production event, left-bottom: cosmic-ray, right-bottom: shower event) The hatched area represents the active volume of the TPC, and the upper and lower sides of each image represent the zenith and nadir directions, respectively.

SMILE-2+ ETCC recorded 4.9×10^7 events after the turn-on. The typical tracks detected during level flight are shown in Fig. 13. Single electron events were selected for the gamma-ray reconstruction as described in 2.2. The measured track images clearly shows what happened in SMILE-2+ ETCC, and enable us to select single-electron events. Thus, the track image itself provides a simple and powerful noise suppression. At the balloon altitudes, cosmic-rays produce positrons or gamma-rays through the interaction with the structure material. Because ETCC is triggered by the coincidence of PSAa and TPC, many cosmic-ray induced events in-

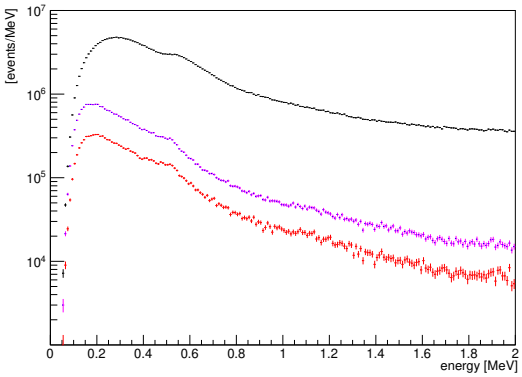

Figure 14. Total energy spectrum of each event selection as described in 2.2 at the level flight. Black, magenta, and red represent the spectra after the event selection of single pixel scintillator hit, fully-contained electron, and Compton scattering kinematics, respectively.

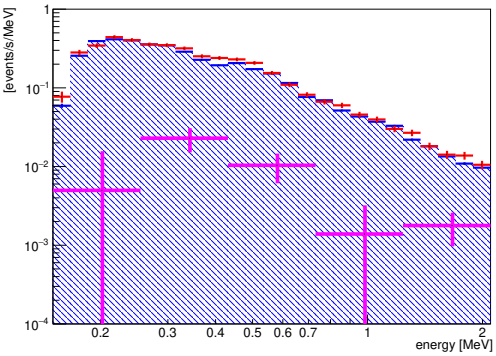

Figure 15. Observed energy spectrum of the ON-region (red), the estimated background (hatch, see text), and the subtraction (magenta).

cluding the electron-positron annihilation line absorbed in PSA were recorded. Using the cosmic-ray or shower events in the flight data, we corrected the gain of the scintillators by the annihilation line every 30 min and that of the TPC by the energy deposition rate of minimum ionizing particles every 10 min. Figure 14 shows the energy spectrum of each event selection during level flight, and after all event selection, 2.4×10^5 events remain. The energy spectrum after the selection of fully-contained electron has a clear excess at 0.511 MeV.

Figure 11 e) shows the light curve obtained by the gamma-ray reconstruction and live-time correction. The gamma-ray event rate is stable at 2.7 Hz at the level flight. When the air mass of the Galactic center is less than 4 g cm^{-2}, the light curve rises with the increase in the elevation angle of the Galactic center. Because the excess at the culmination time of the Galactic center is 0.5 Hz, the estimated intensity of the Galactic center region is $\sim$0.1 photons s^{-1} cm^{-2} sr^{-1} MeV^{-1} with an effective area of 1.5 cm^2 and FoV of 3.1 sr, which is roughly consistent with the measured intensity SPI/*INTEGRAL* (Bouchet et al. 2011), such that the plain, whole detector count rates of SMILE-2+ clearly show an enhancement of gamma-ray emission from the Galactic center region. In contrast, there is no clear excess in Fig. 11 e) at the observation time of the Crab nebula because the flux of the Crab nebula is only $\sim$3% of the photon number of extragalactic diffuse gamma-ray in the FoV of ETCC in an energy range of 0.2–2.1 MeV. We defined the ON-region to the circle centered at the Crab nebula (l = 184.6°, b = -5.8°) with a radius of 40 degrees, which is the HPR of PSF at 0.3 MeV. The obtained spectrum of the ON-region is shown with red in Fig. 15.

4.2. *background estimation*

In the celestial gamma-ray observations at the balloon altitudes, the gamma-ray background comprises extragalactic diffuse gamma-rays, atmospheric gamma-rays, and the instrumental gamma-rays. Although extragalactic diffuse gamma-rays are isotropic at the top of atmosphere, they are scattered and attenuated in the atmosphere at the balloon altitudes. Atmospheric gamma-rays and the instrumental gamma-rays depend on the atmospheric depth, zenith angle, and intensity of cosmic-rays. Unfortunately, the atmospheric depth increased 20% during the observation of the Crab nebula. Hence, we define the OFF-period to 20:30–22:50 ACST on April 7, 2018, when the balloon altitudes decreased the same as that of the Crab observation period (Fig. 9) and there were no bright celestial objects inside the FoV. Figure 16 shows the event intensity map $B(E', \theta')$ in the OFF-period as a function of the detected energy E' and the zenith angle θ'. We assumed this event intensity map as the sky image of background gamma-rays in the horizontal coordinates. Because the zenith angle of the ON-region has a time variation, we calculated the background energy spectrum $g(E')$ with the average during the Crab observation period,

$$g(E') = \frac{1}{T_{\rm obs}} \int_{\rm ON\text{-}region} B(E', \theta'(t)) d\Omega dt, \qquad (7)$$

where $T_{\rm obs}$ is the live time of the Crab observation period, as shown using the hatched spectrum in Fig. 15. The subtraction of the estimated background $g(E')$ from ON-region events is defined $f(E')$, which is the energy spectrum of the gamma-rays from the Crab nebula. The magenta in Fig. 15 shows $f(E')$ as a function of E', and the convoluted significance is 4.0σ. Using the observed data from 08:44 ACST on April 7, 2018 to 06:30 ACST on the next day, we calculated the significance map as

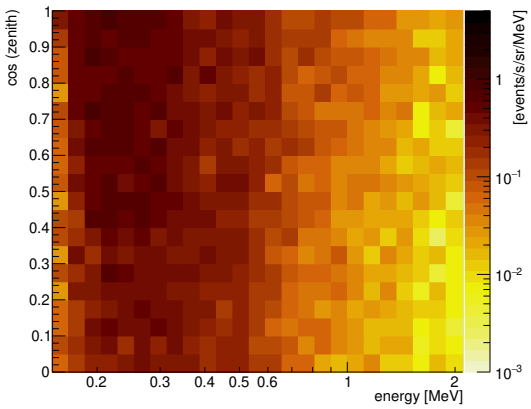

Figure 16. Event intensity map $B(E', \theta')$ in the OFF-period as a function of the detected energy E' and zenith angle θ'.

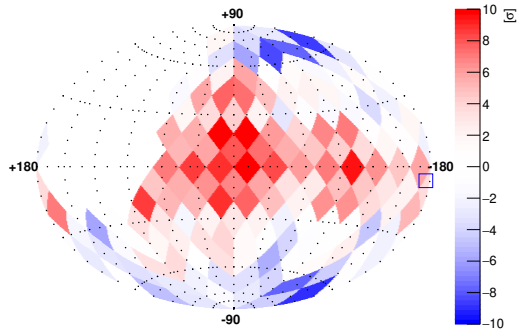

Figure 17. Significance survey map in the galactic coordinates. The open square represents the Crab nebula.

shown in Fig. 17 using the same method. Because the balloon altitude had time variation, we defined $g(E')$ as 10:30–13:30 ACST on April 7, 2018 for an atmospheric depth of less than 3.1 g cm^{-2}, and to 20:30–22:50 ACST on April 7, 2018 for an atmospheric depth of more than 3.1 g cm^{-2}. In addition to the light curve, this figure shows that SMILE-2+ significantly detected the Galactic center region with 10σ. The detailed study of the Galactic center region will be described elsewhere.

4.3. *calculation of flux*

The BG-subtracted spectrum in Fig. 15 includes the detector response and attenuation of atmosphere,

$$f(E') = \frac{1}{T_{\rm obs}} \int f_c(E) A(E, \theta, E', \theta') \exp\left(-\frac{z\tau_{\rm tot}}{\cos\theta}\right) dE dt, \quad (8)$$

where E, θ, A, z, $\tau_{\rm tot}$, and f_c are the true energy and the true zenith angle of the incident photon, the response matrix of the ETCC, the atmospheric depth, the cross

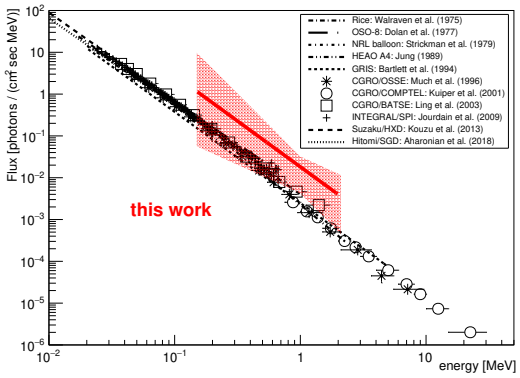

Figure 18. Photon flux of the Crab nebula. Solid line and hatched area are best-fit and statistic error region of 1σ obtained by SMILE-2+, respectively.

section of total attenuation in the atmosphere, and the photon flux of the celestial object, respectively. Using the ETCC simulator described in 2.2, we can estimate $A(E, \theta, E', \theta')$. Because θ, θ', and z have time variations in the actual balloon observation, we calculated the time-averaged response matrix as follows:

$$\bar{R}_{ij} = \frac{1}{T_{\rm obs}} \int A(E_i, \theta, E'_j, \theta') \exp\left(-\frac{z\tau_{\rm tot}}{\cos\theta}\right) dt, \quad (9)$$

where i and j are the number of the energy bin. Then the resultant spectrum is described as

$$f(E'_j) = \sum_i \bar{R}_{ij} f_c(E_i), \quad (10)$$

and f_c can be obtained thorough deconvolution. When we assumed a single power-law for f_c, a deconvoluted photon flux of $(1.82 \pm 1.40) \times 10^{-2}\,(E/\mathrm{MeV})^{-2.19\pm0.82}$ photons s^{-1} cm^{-2} MeV^{-1} was obtained. This spectrum is shown in Fig. 18 together with 1σ error band. According to the *Swift*/BAT transient monitor (Krimm et al. 2013), there were no significant flares during the observation time[2]. Therefore we can compare our result with other observations of the Crab nebula for consistency check. Our result is consistent with those previous observations of the Crab nebula.

To investigate any time-dependence of the OFF-period, photon fluxes for two more background periods were calculated. One was defined at 10:30–13:30 ACST on April 7, 2018. The atmospheric depth of this period was 3.01 g cm^{-2}, which was 13% thinner than that of the Crab observation period (14:30–19:30 ACST on April 7, 2018). It means the intensity of atmospheric gamma-rays should decrease. The resulting gamma-ray

[2] https://swift.gsfc.nasa.gov/results/transients/index.html

Table 1. Obtained parameters with the different background time

BG time[a]	20:30–22:50	10:30–13:30	14:30–19:30
normalization[b]	1.82 ± 1.40	2.08 ± 1.38	1.55 ± 1.37
photon index	2.19 ± 0.82	2.28 ± 0.81	2.05 ± 0.80
significance	4.0σ	6.6σ	2.9σ

[a] time on April 7, 2018 in ACST

[b] unit in 10^{-2} photons s^{-1} cm^{-2} MeV^{-1}

flux of the Crab nebula based on this background period becomes an overestimation. Another period was defined at the Crab observation period. This selection can be justified because the flux of the Crab nebula is negligible in comparison with the intensity of extragalactic diffuse and atmospheric gamma-rays on the inside of the ETCC FoV. Using the same method used for the original background period, single power-law spectra for these additional two background period were calculated. The obtained parameters are listed in Table 18. There is no large difference between these parameters, and the obtained photon flux was found to have little dependence on the selection of the OFF-period.

5. DISCUSSION

Generally, the detection sensitivity $S(E)$ in some energy band is defined by the detectable flux with the significance of 3σ, the observation time of 10^6 s, and the energy window $\Delta E = E$. The background rate of SMILE-2+ is estimated by eq. (7), the detection sensitivity of SMILE-2+ is described by

$$S(E) = \frac{3\sqrt{T_{\rm obs} \int B(E', \theta') dE' d\Omega'}}{T_{\rm obs} \int A(E, 0°, E', \theta') dE' d\Omega'}, \qquad (11)$$

in the zenith direction ($\theta = 0°$). When $d\Omega$ is defined by the half power radius shown in Fig. 7, the detection sensitivity of SMILE-2+ is the blue long-dashed line in Fig. 19. The realized sensitivity is approximately ten times higher than that of SMILE-I, which detected the Crab nebula within a few hours.

The background events comprise extragalactic diffuse gamma-ray, atmospheric gamma-ray, instrumental gamma-rays, and the other particles (e.g., neutron). Radioactivation is negligible because the duration time is too short in balloon observation. Therefore the background event intensity $B(E', \theta')$ will be described as

$$B(E', \theta') = \int (I_c + I_a) A(E, \theta, E', \theta') dE d\Omega + B_{\rm instr}, \qquad (12)$$

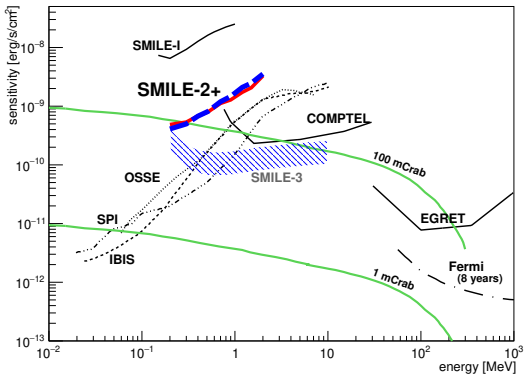

Figure 19. 3 σ detection sensitivity of SMILE-2+ for the continuum spectrum with the observation time of 10^6 s and the energy window $\Delta E = E$. The blue long-dashed line represents the realized sensitivity based on the actual background event intensity. When the background photons comprises extragalactic diffuse, atmospheric gamma-rays, and the instrumental background, the sensitivity is estimated at the red solid line. In the next observation SMILE-3, the estimated detection sensitivity is represented by the blue hatched area. The uncertainty of SMILE-3 sensitivity depends on cutoff rigidity, balloon altitude, and solar modulation. The black lines represent the previous results (Attwood et al. 2009; Takahashi et al. 2013; Takada et al. 2011).

where I_c and I_a are intensities of extragalactic diffuse gamma-ray and atmospheric gamma-ray respectively, and $B_{\rm instr}(E', \theta')$ is the event intensity of the instrumental background. The intensity of extragalactic diffuse gamma-ray has a zenith angle dependence based on the atmospheric attenuation and scattering at the balloon altitudes (Makino 1970; Horstman & Horstman-Moretti 1971; Schönfelder et al. 1977; Takada et al. 2011), whereas it is uniform at the top of the atmosphere. The atmospheric gamma-rays, which are produced by the interaction between cosmic-rays and atmosphere, also have a dependence on the atmospheric depth, cutoff rigidity, and solar modulation. There are some models for the atmospheric gamma-rays. PARMA (Sato et al. 2008) is an analytical model based on the simulation using PHITS (Iwase et al. 2002), as a function of energy, zenith angle, atmospheric depth, solar modulation, and cutoff rigidity. However, this model does not consider the primary cosmic electron/positron as the initial particles. Ling (1975) and Ling et al. (1977) is a semiempirical model including extragalactic diffuse gamma-ray based on some balloon observations as a function of energy, zenith angle and atmospheric depth. This semiempirical model did not consider the dependence on cutoff rigidity and solar modulation, whereas this model is cited by many observations.

For the intensity model of the extragalactic diffuse and atmospheric gamma-rays, we adopted Ling (1975) and Ling et al. (1977) scaled with the dependence of cutoff rigidity and solar modulation. As the correction of the cutoff rigidity, we scaled the models with $(4.5\ \mathrm{GV}/8.4\ \mathrm{GV})^{1.13}$. In contrast, the balloons referred by Ling's models were launched around solar maximum and SMILE-2+ was launched near solar minimum. The atmospheric gamma-ray intensity at solar minimum is estimated to 1.2–2.0 times larger than that at the solar maximum (Morris 1984; Sazonov et al. 2007), we thus scaled the intensity of atmospheric gamma-ray by 1.2. Assuming the gamma-ray intensity at the atmospheric depth of 3.0 g cm^{-2}, SMILE-2+ ETCC is expected to obtain the spectrum shown with filled triangle in Fig. 20. To evaluate the instrumental background $B_{\mathrm{intsr}}(E', \theta')$, we simulated the reconstructed events utilizing the ETCC simulator under the initial particle (proton, neutron, electron, and positron) calculated by PARMA. The filled circle in Fig. 20 represents the estimated energy spectrum of instrumental background at the same altitude. The amount of instrumental background is one-half of that of the essential background comprised extragalactic diffuse and atmospheric gamma-rays; Thus the instrumental background have affected very little the detection sensitivity of SMILE-2+. The expected total background spectrum, which is shown with the hatched area in Fig. 20, approximately consistent with the actual observed energy spectrum shown with open square in Fig. 20. Using this estimated total background, we can obtain the detection sensitivity independent of the realized sensitivity mentioned above. The estimated detection sensitivity of SMILE-2+ as shown in the red solid line in Fig. 19 is also consistent with the realized sensitivity.

These results mean that the background spectrum and the detection sensitivity of observation utilizing an ETCC in space are well understood in the results of the ground calibrations, whereas most of conventional Compton camera like COMPTEL has an achieved sensitivity of several times worse than the expectation (Schönfelder 2004; Bandstra et al. 2011). Independently, the enhancement of the light curve at the culmination time of the Galactic center strongly supports this estimation. If the instrumental background were several times intense than extragalactic gamma-rays such as COMPTEL, we could not observe this enhancement. The majority of the instrumental background in the observation using an ETCC is composed of gamma-rays generated by the interaction between the instrumental material and cosmic rays because the ETCC has some powerful background rejection tools like particle identification, track image, and Compton kinematics test. The upward instrumental gamma-rays are intense owing to the amount of material below the ETCC. However, the ETCC can decide the direction of the incident gamma-ray to a point, event by event, SMILE-2+ can suppress the instrumental background in the FoV to the contamination expected with the PSF. By this noise condition, it also becomes easy and reliable to estimate the detection sensitivity of next observation (SMILE-3). When we construct a new TPC with a volume of $30 \times 30 \times 30$ cm^3 filled by a CF_4 gas with a pressure of 3 atm and optimize the structure design, the ETCC will have an effective area of approximately 10 cm^2 for 0.4 MeV and 1 cm^2 for 2.5 MeV. For improving a PSF, we are developing an analysis using machine learning, and the first trial of deep learning for the recoil direction and scattering point provides twice better PSF than that described by this paper (Ikeda et al. 2021). If the direction accuracy of Compton-recoil electron could be improved to the limitation of the multiple scattering, the PSF of ETCC will improve to 10 degrees for 0.4 MeV and 2 degrees for 2.5 MeV at HPR. With utilizing such an ETCC loaded on a long-duration balloon (SMILE-3), the expected detection sensitivity will achieve several higher than that of COMPTEL as shown with the blue hatched area in Fig. 19. Recently, a super-pressure balloon can be launched with a duration time over one month at the middle latitude in the southern hemisphere (Kierans et al. 2017). Therefore, if we will launch an updated ETCC using a long-duration balloon, SMILE-3 can have a significant progress from the observation of

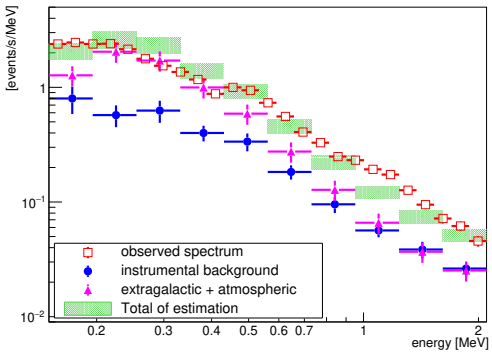

Figure 20. Energy spectra within the zenith angle of 60 degrees at the atmospheric depth of 3.0 g cm^{-2}. Open square is the detected events during 10:30–13:30 ACST on April 7 (ACST), 2018. The filled circles, filled triangles and hatched areas represent the estimated instrumental background, the summation of extragalactic diffuse and atmospheric gamma-ray component based on Ling model (Ling 1975; Ling et al. 1977), and the total estimated spectrum, respectively.

COMPTEL because of the observation time of $\sim 10^6$ s realized by the large FoV of ETCC.

6. SUMMARY

For progress in MeV gamma-ray astronomy, we are developing an ETCC having the ability of imaging spectroscopy based on a proper PSF and powerful background rejection tools due to particle identification, Compton-scattering kinematics test, and charged particle track imaging. A proper PSF of ETCC enables us to obtain the energy spectrum of the observation target by the simple ON-OFF method. In 2018, we launched the second balloon SMILE-2+ for confirming the observations of celestial objects. The ETCC loaded on SMILE-2+ has an effective area of 1.1 cm^2 for 0.356 MeV, the PSF of 30 degrees for 0.662 MeV at HPR, and the FoV of 3.1 sr utilizing the TPC with a volume of $30\times30\times30$ cm^3 filled with an argon gas at the pressure of 2 atm. SMILE-2+ detected gamma-rays from the Crab nebula with a significance of 4.0σ. Obtained flux is consistent with other observations. Thus, SMILE-2+ has attained to apply the imaging spectroscopy based on a proper PSF in MeV gamma-ray astronomy for the first time. In addition, the light curve and the significance survey map show that the Galactic center region is very bright with the significance of 10σ at the energy range of 0.2–2.1 MeV. The observed energy spectrum during the level flight was explained by the background containing extragalactic diffuse, atmospheric, and instrumental gamma-rays. The achieved detection sensitivity of SMILE-2+ is consistent with the estimated sensitivity based on the ground calibrations, whereas most of conventional Compton cameras have only achieved sensitivity several times worse than the expectation. The instrumental gamma-rays have affected little the detection sensitivity of SMILE-2+, because the instrumental gamma-rays constitute only one-third of the background. This fact demonstrates that ETCC overcomes the background problem and it is most important to estimate sensitivity with a PSF (not an ARM) in the design of a Compton camera similar to the other telescopes in X-ray or GeV bands. In the near future, we will update the ETCC having an effective area of approximately 10 cm^2 and a PSF of several degrees at HPR, and will launch a long-duration balloon for the scientific observation as SMILE-3. The ETCC would become a unique pioneer with a deeper survey than COMPTEL in MeV gamma-ray astronomy.

The balloon-borne experiment was conducted by Scientific Ballooning (DAIKIKYU) Research and Operation Group, ISAS, JAXA. This study was supported by the Japan Society for the Promotion of Science (JSPS) Grant-in-Aid for Scientific Research (S) (21224005), (A) (20244026, 16H02185), Grant-in-Aid for Young Scientists(B) (15K17608), JSPS Grant-in-Aid for Challenging Exploratory Research (23654067, 25610042, 16K13785, 20K20428), a Grant-in-Aid from the Global COE program "Next Generation Physics, Spun from Universality and Emergence" from the Ministry of Education, Culture, Sports, Science and Technology (MEXT) of Japan, and Grant-in-Aid for JSPS Fellows (16J08498, 18J20107, 19J11323). Some of the electronics development was supported by KEK-DTP and Open-It Consortium. And we thank Enago (www.enago.jp) for the English language review.

REFERENCES

Agostinelli, S., et al. 2003, Nucl. Instr. Meth. A, 506, 250
Aharonian, F., et al., 2018, PASJ, 70, 113
Aprile, E., et al. 2008, Nucl. Instr. Meth. A, 593, 414
Attwood, W. B., et al., 2009, ApJ, 697, 1071
von Ballmoos, P. 1995, Exp. Astron., 6, 85
Bandstra, M. S., et al. 2011, ApJ, 738, 8
Bartlett, L. M., et al., 1994, AIP Conf. Proc., 304, 67
Boggs, S. E., et al. 2000, ApJ, 544, 320
Bouchet, L., et al. 2008, ApJ, 679, 1315
Bouchet, L., et al., 2011, ApJ, 739, 29
Briggs. M. S., et al. 1999, ApJ, 524, 82
Carr, B. J., et al. 2010, PhRvD, 81, 104019
Churazov, E., et al. 2015, ApJ, 812, 62
Deaorgher, L., et al. 2005, JMPA, 20, 6802
Diehl, R., et al. 2015, Science, 345, 1162
Diehl, R., et al. 2018, A&A, 611, 12
Dolan, J. F., et al., 1977, ApJ, 217, 809
Dujmic, D., et al., 2008, Nucl. Instr. Meth. A, 584, 327
Hamaguchi, K., et al., 2019, BAAS, 51, 145
Horstman, H., & Horstman-Moretti, E. 1971, Nature, 229, 148
Ikeda, T., et al., 2021, submitted in PTEP (arXiv:2105.0251)
Iwase, H., Niita, K., & Nakamura, T., 2002, J. Nucl. Sci. Technol. 39, 1142
Jourdain, E., & Roques, J. P., 2009, ApJ, 704, 17
Jung, G. V., 1989, A&A, 338, 972
Kamiya, K 2011, Ph.D. University of California
Kierans, C., et al., 2017, PoS, INTEGRAL2016, 075
Kouzu, T., et al., 2013, PASJ, 65, 74

Krimm, H. A., et al., 2013, ApJS, 209, 14
Kuiper, L., et al., 2001, A&A, 378, 918
Ling, J. C. 1975, J. Geophys. Res., 80, 3241
Ling, J. C., et al., 1977, J. Geophys. Res., 82, 1463
Ling, J. C., & Wheaton, Wm. A., 2003, ApJ, 598, 334
Mahadevan, R., Narayan, R., & Krolik, J. 1997, ApJ, 486, 268
Makino, F. 1970, Ap&SS, 8, 251
Matz, S. M., et al. 1988, Nature, 331, 416
McConnell, M. L., et al. 1996, A&AS, 120, 149
Mészáros, P., & Rees, M. J. 2010, ApJ, 715, 967
Mizumoto, T., et al. 2015, Nucl. Instr. Meth. A, 800, 40
Morris, D. J., 1984, J. Geophys. Res., 89, 10685
Much, R., et al., 1996, A&A, 120, 703
Ochi, A., et al. 2001, Nucl. Instr. Meth. A, 471, 264
Prantzos, N., et al. 2011, RvMP, 83, 1001
Sato, T., et al. 2008, Radiation Research, 170, 244
Sauli, F. 1997, Nucl. Instr. Meth. A, 386, 531
Sazonov, S., et al., 2007, MNRAS, 377, 1726
Schönfelder, V., Graser, U., & Daugherty, J. 1977, ApJ, 217, 306
Schönfelder, V., et al. 1993, ApJS, 86, 657
Schönfelder, V., et al. 2000, A&AS, 143, 145
Schönfelder, V. 2004, New Astron. Rev., 48, 193
Sekiya, H., et al. 2006, Nucl. Instr. Meth. A, 563, 49
Strickman, M. S., Johnson, W. N., & Kurfess, J. D., ApJ, 230, L15
Strong, A. W., Moskalenko, I. V., & Reimer, O. 2000, ApJ, 537, 763
Takada, A., et al. 2005, Nucl. Instr. Meth. A, 546, 258
Takada, A., et al. 2011, ApJ, 733, 13
Takahashi, T., et al., 2013, APh, 43, 142
Tamagawa, T., et al. 2006, Nucl. Instr. Meth. A, 560, 418
Tanimori, T., et al. 2004, New Astron. Rev., 48, 263
Tanimori, T., et al. 2015, ApJ, 810, 28
Tanimori, T., et al. 2017, Scientific Reports, 7, 41511
Thompson, D. J., Simpson, G. A., & Özel, M. E. 1981, J. Geophys. Res., 86, 1265
Toma, K., et al. 2011, ApJ, 731, 127
Trombka, J. I., et al., 1973, ApJ, 181, 737
Urry, C. M., & Padovani, P. 1995, PASP, 107, 803
Walraven, G. D., et al., 1975, ApJ, 202, 502
Weidenspointner, G., et al. 2001, A&A, 368, 347